








Interband response of type-II quantum cascade detectors [Invited]

STEFANIA ISCERI,¹  ANDREAS WINDISCHHOFER,¹ MIRIAM GIPARAKIS,² ROLF SZEDLAK,¹ WERNER SCHRENK,³  GOTTFRIED STRASSER,¹  BENEDIKT SCHWARZ,¹  AND AARON MAXWELL ANDREWS^{1,*} 

¹Institute of Solid State Electronics E362, Technische Universität Wien, 1040 Vienna, Austria

²Photonics Institute E387, Technische Universität Wien, 1040 Vienna, Austria

³Center for Micro- and Nanostructures E057-12, Technische Universität Wien, 1040 Vienna, Austria

*aaron.andrews@tuwien.ac.at

Abstract: Quantum cascade detectors (QCDs) are room-temperature photovoltaic infrared devices based on intersubband transitions. In this work, we expand the mid-infrared QCD functionality by utilizing the interband (IB) transitions in the extractor region to realize a detector also in the short-wavelength infrared region of the electromagnetic spectrum. We investigate this scheme with simulations and characterization of the IB transitions in type-II InAs/AlSb QCD structures on GaSb substrates. We compare four different QCD devices with IB transitions between 1.83 μm and 2.33 μm . The measured peak responsivities at zero bias are 2.8 – 24.8 mA W^{-1} with specific detectivities between 2.56×10^7 – 1.68×10^8 Jones. A detailed analysis of the devices under an applied bias shows that the IB response increases up to 330 times at a bias of 1.0 V and 360 times at a bias of -1.0 V.

Published by Optica Publishing Group under the terms of the [Creative Commons Attribution 4.0 License](https://creativecommons.org/licenses/by/4.0/). Further distribution of this work must maintain attribution to the author(s) and the published article's title, journal citation, and DOI.

1. Introduction

Mid-infrared (MIR) and short-wavelength infrared (SWIR) sources and detectors are essential for applications in spectroscopy [1,2], chemical sensing [3,4], biological imaging, astronomy [5–10], free-space optical communication [11], integrated photonics [4], and characterization of frequency combs [2,12–14]. Hofstetter *et al.* demonstrated that unbiased quantum cascade lasers (QCLs) can act as a intersubband (ISB) photovoltaic detector [15], the QCD. The QCD is designed so that a photon with the target energy excites an electron from the lower bound state to an upper level in the conduction band (CB). The electron is removed from the excited level by the cascading extractor region, eventually reaching the ground level of the next cascade and contributing to the photocurrent [15–19]. Following the ISB selection rule in the CB, QCDs are only sensitive to light polarized in the growth direction, contrary to IB transitions, which are sensitive to both polarizations. QCDs were shown in the MIR [4,15,20,21] and near-infrared (NIR) spectral range [22,23] at room temperature and in the THz range [24–26] at cryogenic temperatures. QCDs are zero bias detectors and therefore have a low dark current [15]. This contrasts with quantum well intersubband photodetectors (QWIPs), which are infrared photodetectors based on biased superlattices (SLs) where an electron is excited from a bound state to the CB continuum [18,27,28]. QWIPs exhibit high responsivities; however, they have a thermally activated dark current above 100 K [17,29].

The QCD dual functionality presented here is inspired by other type-II photodetectors. Type-II superlattice (T2SL) detectors have been employed for the detection range from SWIR to MIR [30–32]. They are based on the InAs/GaSb, InAs/GaSb/AlSb [32], and InAs/InAs_{1-x}Sb_x material

systems [30]. The interband cascade infrared photodetector (ICIP) is also a type-II multistage infrared detector [33], operating in the SWIR [34], MIR [35–38], and long-wavelength infrared (LWIR) [39–42]. In an ICIP, carriers are generated in SL absorption regions, which are combined with cascade regions to act as electron and hole blocking layers [43–45]. The electrons then move through the extraction region and recombine with the holes generated in the next period [33,44].

The main figures of merit for photodetectors are the responsivity and the detectivity. The responsivity is defined as the electrical output per optical input power [46]:

$$R = \frac{I}{P} = \frac{\lambda q \eta p_e}{hc N} \quad (1)$$

where λ is the wavelength, q is the elementary charge, h is Planck's constant, c is the speed of light, η is the absorption efficiency, p_e is the extraction efficiency, and N is the number of cascades. The detectivity is the signal-to-noise behavior. For QCDs in dark and illuminated conditions, at any bias and temperature, the specific detectivity can be expressed as [19,47]:

$$D^* = R / \sqrt{2e \frac{1}{N} |J| + \frac{4k_B T}{dV}} \quad (2)$$

where J is the density of the total current density, without distinction between illuminated and dark conditions, V is the bias, k_B is Boltzmann constant, and T the operating temperature. A trade-off between responsivity and detectivity must be found by optimizing the number of periods N , the barrier thickness, and the absorption efficiency η . An optimum can be achieved through quantum design and engineering [3,23,48]. For the same doping density, η is inversely proportional to the effective mass m_e^* of the well material [18,49]. A lower effective mass also leads to a reduction in scattering rates, which increase resistance and reduce noise, and consequently improve specific detectivity [50].

Typically, the QCD active region is based on an ISB vertical transition, and higher photon energies require a material system with a higher conduction band offset (CBO). For longer wavelengths, a diagonal transition design is more favorable because it does not rely on resonant tunneling [46]. The most widely used material system for QCDs is InGaAs/InAlAs lattice-matched to InP substrates [51]. Other materials, such as ZnCdSe/ZnCdMgSe and GaN/AlGaIn, benefit of a higher CBOs [20,21,52] for excellent detectivity, but have poor responsivity due to the high electron effective mass m_e^* . The InAs/AlAsSb material system offers the advantages of a CBO up to 2.28 eV [51] and low electron effective masses of InAs $m_e^*=0.026m_0$ and AlSb $m_e^*=0.140m_0$ [51]. InAs/AlAsSb can be grown lattice-matched to InAs substrates [49,53] or strain-compensated on GaSb substrates [54]. For GaSb substrates ($E_g=0.73$ eV), SWIR devices can be processed in the 45° polished facet mesa configuration for backside illumination, while InAs substrates absorb photon energies higher than 0.35 eV [49,53,55]. Schwarz *et al.* demonstrated a single period QCD resulting in an increased responsivity up to 1.3 A W⁻¹ thanks to the reduction of the series resistance [56,57]. To improve responsivity, normal incident sensitivity, and noise performances, various incoupling methods have been demonstrated [55,58–61].

In this work, we demonstrate a novel type of photodetector based on the IB response of InAs/AlSb QCDs as a way to realize a dual-wavelength operation. This is obtained by stimulating the IB absorption of QCD structures independent of the ISB absorption, pushing the detection region to the SWIR regime ($\lambda=1.4 - 3.0 \mu\text{m}$). The ISB response of the devices presented here was reported in [54]. The ISB and IB absorptions are simulated as a function of an applied electric field, and the main transitions are identified in the band structure. Then, the responsivity and noise of the IB absorption of the devices are characterized as a function of the applied bias voltage.

2. Results and discussion

Four different QCDs were designed using a four-band $\mathbf{k} \cdot \mathbf{p}$ formalism, including scattering mechanisms such as longitudinal optical (LO) and acoustic phonon scattering and interface roughness scattering [62]. The ISB transitions are engineered at 3.65 μm (design A), 4.30 μm (design B), 4.30 μm (design C), and 5.50 μm (design D), as discussed in [54].

The InAs/AlSb QCDs were grown strain-balanced to GaSb substrates by molecular beam epitaxy (MBE) using a Riber Compact 21 system and n-type doped with Te [54]. Active regions have a total of 20 periods. The samples were then fabricated into $150 \times 150 \mu\text{m}^2$ mesas, using UV lithography and reactive ion etching. The top contact (10/380 nm Ti/Au) and backside bottom contact (10/380 nm Ti/Au) were deposited using sputtering. The QCDs were then cleaved and polished to produce a 45 $^\circ$ -facet double-pass geometry [14,23,53]. Finally, they were soldered to a copper base plate and bonded to a printed circuit board.

Figure 1 shows the simulated band structures of device D ($\lambda_{ISB}=5.50 \mu\text{m}$) with different applied electric field values, equal to (a) -16 kV cm^{-1} , (b) 0 kV cm^{-1} , and (c) 16 kV cm^{-1} . The modeled electric field is approximately the maximum measured for the devices, discussed later. For normal QCD operation, the designed ISB transition is denoted by a black arrow in (b). The states involved in the IB transitions giving the strongest absorption are drawn with bold lines. The simulation results suggest that IB absorption is primarily driven by transitions involving hole states located below the valence band edge, rather than near-edge states. For negative electric field values, the CB states have a lower energy separation and a higher overlap. The energy spread of the states in the miniband of the CB is larger with an applied positive electric field. In the SWIR region, the ISB absorption is not required for electrons to travel throughout the active region (AR). Under bias, holes are also mobile and can travel through the valence band (VB) states.

Figure 2(a) shows the sum of the modeled absorption transitions of transverse-magnetic (TM) and transverse-electric (TE) modes as a function of the wavenumber (wavelength) for the three different electric field values ($-16, 0, \text{ and } 16 \text{ kV cm}^{-1}$) of device D ($\lambda_{ISB}=5.50 \mu\text{m}$). The simulation shows the absorption probability and does not involve the extraction efficiency, despite the latter also contributes positively to the measured detectors' responsivity. The dashed vertical line at 3700 cm^{-1} ($2.70 \mu\text{m}$) indicates the cutoff wavenumber (wavelength) of the N-BK7 plano-convex lens used later in the experimental setup to select only the IB transitions. A simulation of optical absorption including the conduction and valence band states shows the expected ISB transitions for which the QCD was designed and which were not experimentally characterized in this work. Note that absorption depends on polarization, where the ISB absorption is sensitive only to light polarized in the growth direction (out-of-plane) and the IB absorption can detect both in-plane and out-of-plane polarizations. The intensity of the individual ISB absorption transitions is influenced by the electric field. A weak TM-polarized absorption transition also occurs at $3.47 \mu\text{m}$. Upon the application of a positive and a negative electric field, the intensity of the IB absorption increases. If a positive (negative) bias is applied, the main absorption peak is at a higher (lower) energy. Figure 2(b, c, d) shows the dominant contributions to the absorption response per single transition at three different values of the electric field. The solid blue lines represent the ISB transitions, the purple dashed lines represent the IB transitions. We observe that different transitions are involved in the absorption at different electric field values. Shifts in detection energies are attributed to these different transitions.

The QCDs were characterized electrically and optically in the SWIR. Current [A]/ current density [A/cm^2] was measured as a function of bias voltage (I-V) with a Keithley 2612B source meter under illuminated and dark conditions to extract the differential resistance of the four different QCD designs studied (Fig. 3). The asymmetry of the plots is due to the asymmetry of the design of the band structure. The observed difference in current under dark and illuminated conditions reflects the transport of photogenerated carriers across successive periods of the QCDs.

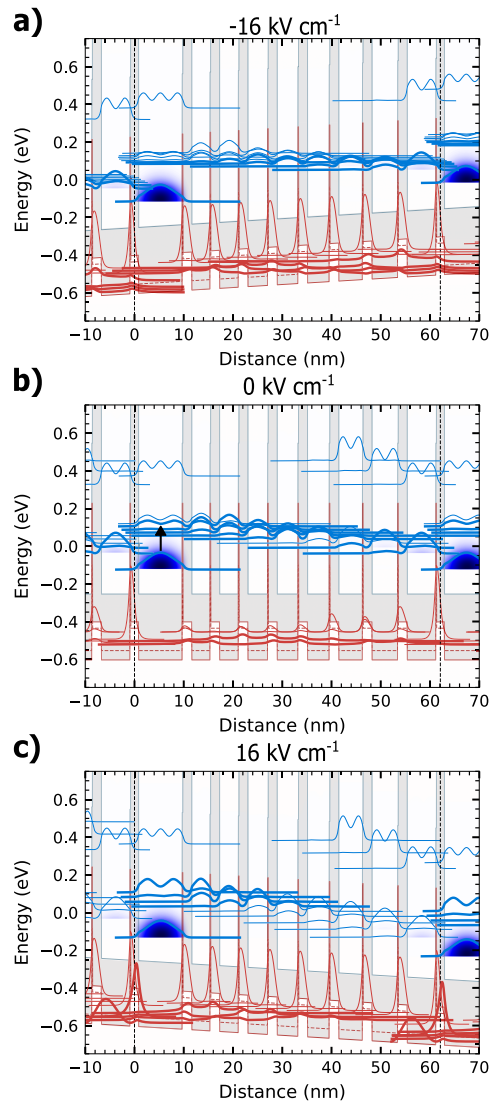


Fig. 1. Band diagram at three different applied bias fields: (a) -16 kV cm^{-1} , (b) 0 kV cm^{-1} , and (c) 16 kV cm^{-1} for the design D ($\lambda_{ISB}=5.50 \mu\text{m}$). The conduction band edge is displayed in dark gray, the heavy-hole valence band is in solid red, the light-hole valence band is in dashed red, and the band gap is colored in light gray. The red peaks reaching on the left of each InAs conduction band are the valence bands of submonolayer InSb layers grown for strain-compensation. The probability densities are represented in blue and red for electrons and holes, respectively. The blue filled area of the wavefunction in the broadest quantum well (QW) corresponds to the electron population. The ISB transition is denoted by a black arrow in (b). The states involved in the IB transitions are drawn with bold lines, while the remaining wave functions are drawn with thin lines.

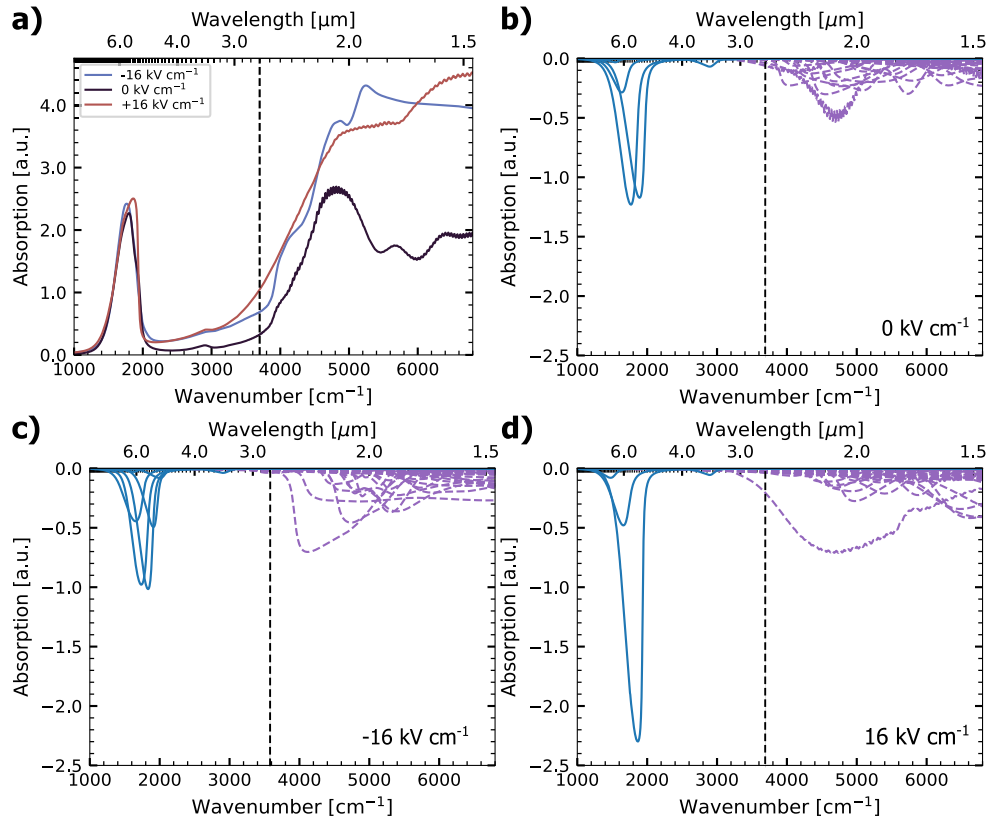


Fig. 2. (a) Sum of individual simulated absorption spectra (TE and TM contributions) as a function of the wavenumber (wavelength) for three different electric field values (-16 , 0 , and 16 kV cm^{-1}) of device D ($\lambda_{ISB}=5.50 \mu\text{m}$). (b, c, d) Simulated absorption per transition as a function of the wavenumber (wavelength). The blue solid lines represent the ISB transitions, the purple dashed lines represent the IB transitions. The dashed vertical lines represent the cutoff wavelength given by the lens used in the experimental setup to select only the IB transitions.

The SWIR spectral characterization of the QCDs was performed using a Bruker Vertex 70v Fourier transform infrared spectrometer (FTIR) and a tungsten lamp. An N-BK7 plano-convex lens was used to block the signal at wavelengths longer than $2.70 \mu\text{m}$, so that the ISB transitions of the designs were not stimulated. A Stanford Research Systems SR570 transimpedance amplifier was used to measure photocurrent. The beam spot of the tungsten lamp was measured with an automated XY stage using the QCD (see Figure S1 in the [Supplement 1](#)) and calibrated with a Thorlabs PM100D optical power meter.

The room-temperature responsivities and detectivities of the IB absorption of the QCDs at zero bias are: 2.78 mA W^{-1} and 2.56×10^7 Jones (device A), 15.81 mA W^{-1} and 8.87×10^7 Jones (device B), 24.80 mA W^{-1} and 1.68×10^8 Jones (device C), and 11.91 mA W^{-1} and 2.49×10^7 Jones (device D). To determine the detectivity, the noise current was measured under dark conditions and found to be in good agreement with the calculated values (see [Supplement 1](#)).

The influence of bias on the four devices was investigated. Figure 4 shows the responsivity spectra at different bias voltages, ranging between -1.0 V and 1.0 V , of the four QCD structures. The responsivity spectra were fitted with multiple Gaussian functions to obtain the peak positions. Different transitions were identified for the designs and summarized in Table 1. Under bias,

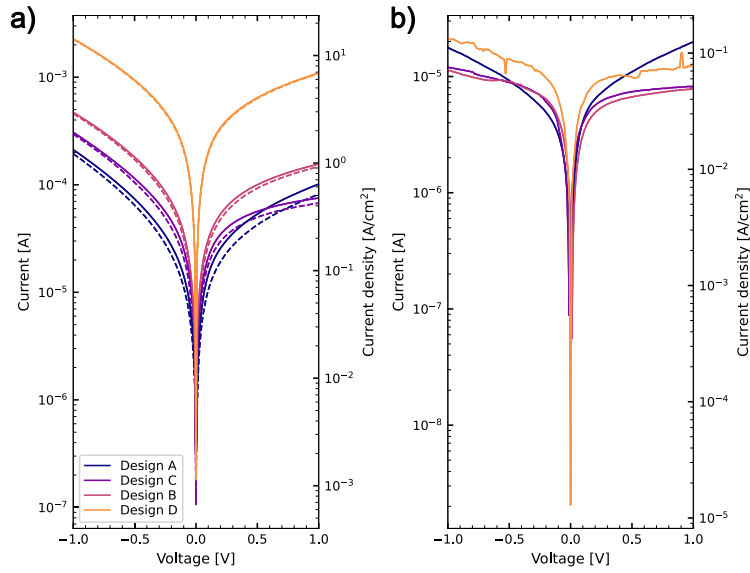


Fig. 3. (a) Current (left y-axis) and current density (right y-axis) versus bias voltage (I-V) curve plots for the different QCD designs in illuminated (continuous line) and dark (dash line) conditions. The devices were illuminated with the NIR source of the FTIR. (b) Difference between illuminated and dark current (left y-axis) and current density (right y-axis) versus bias voltage.

the operation of the devices is photoconductive and no longer photovoltaic. The holes can now cascade through the VB of the entire active region.

Table 1. Summary of the IB absorption peaks (λ_{IB1} , λ_{IB2} , λ_{IB3}) from fitting the four different QCDs included in this study with +1 V, 0 V, and -1 V. The responsivity curves are fitted with a multiple Gaussian function

Design (λ_{ISB})	Bias	λ_{IB1} [μm]	λ_{IB2} [μm]	λ_{IB3} [μm]	ν_{IB1} [cm^{-1}]	ν_{IB2} [cm^{-1}]	ν_{IB3} [cm^{-1}]	Responsivity [A W^{-1}]	Detectivity [Jones]
A (3.65 μm)	+	1.87	2.02	2.32	5335	4944	4307	0.993	6.702×10^9
	0	1.86	2.18		5382	4586		0.003	2.561×10^7
	-	1.87	2.00	2.29	5357	4995	4369	0.923	3.814×10^9
B (4.30 μm)	+	1.84	1.94	2.20	5430	5155	4555	0.347	1.594×10^9
	0		1.94	2.38		5157	4208	0.016	8.869×10^7
	-	1.83	1.93	2.16	5451	5183	4619	0.535	1.516×10^9
C (4.30 μm)	+	1.89	2.06	2.29	5285	4849	4367	0.373	2.179×10^9
	0	1.84	2.25		5439	4447		0.025	1.682×10^8
	-	1.92	2.10	2.29	5261	4768	4376	0.559	1.926×10^9
D (5.50 μm)	+	1.92	2.07	2.50	5199	4834	4061	0.541	9.297×10^8
	0	1.91	2.78		5243	3593		0.012	2.488×10^7
	-	1.91	2.05	2.41	5222	4881	4145	0.994	1.309×10^9

The measured transition wavelengths for the negative bias are shorter, red-shifted, than for the positive bias, except for Device C. This allows detector tunability approaching 1100 cm^{-1} . The room-temperature responsivities of the IB peaks of the QCD structures increase up to 0.99 A W^{-1} at 1.0 V and 0.92 A W^{-1} at -1.0 V (Design A), 0.35 A W^{-1} at 1.0 V and 0.53 A W^{-1} at -1.0 V

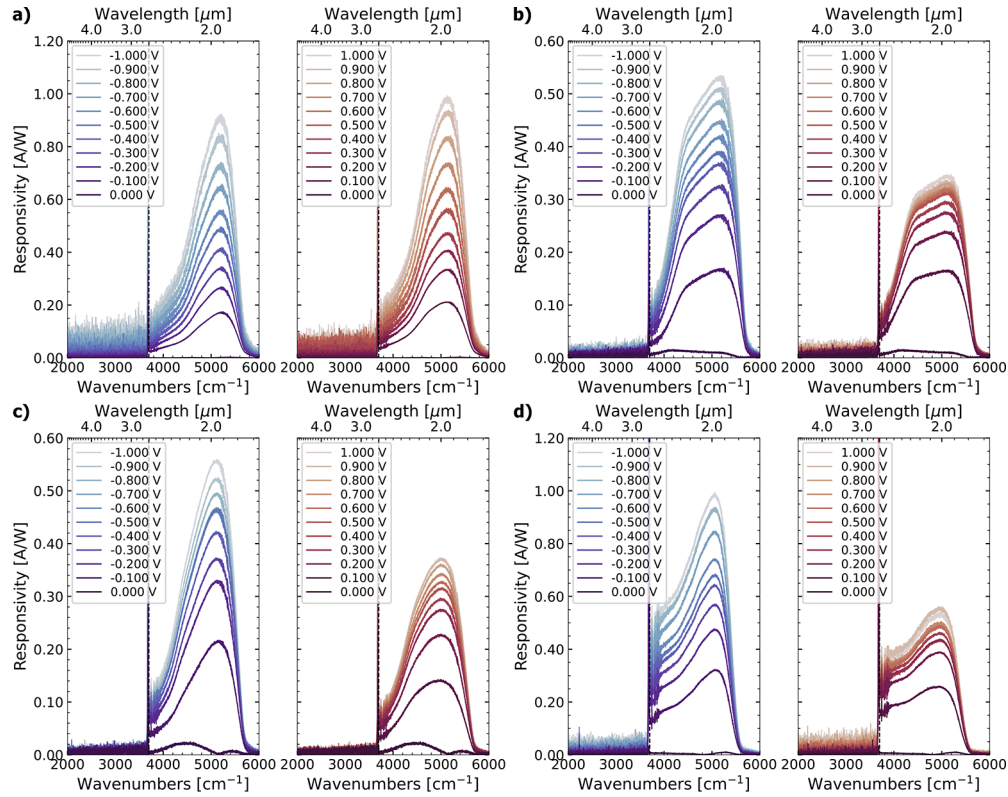


Fig. 4. Responsivity measurements at different bias voltage, ranging between -1.0 V and 1.0 V, of the four QCDs with a designed ISB transition λ_{ISB} at (a) 3.65 μm , (b) 4.30 μm , (c) 4.30 μm , and (d) 5.50 μm . The vertical dashed line indicates the cutoff wavelength of the lens used to select only the interband transitions and prevent the excitation of the ISB transitions. The responsivity curves are fitted with a multi-Gaussian function.

(Design B), 0.37 A W^{-1} at 1.0 V and 0.56 A W^{-1} at -1.0 V (Design C), and 0.54 A W^{-1} at 1.0 V and 0.99 A W^{-1} at -1.0 V (Design D). In the case of Device A, the measurements show that the responsivity increases by up to 330 times for -1.0 V and 360 times for 1.0 V. This value is much higher than the increase in absorption shown in the simulation due to the AR extraction efficiency, which positively influence the responsivity of the detector.

The room-temperature IB responsivities and detectivities in the SWIR range of our devices are lower than those of commercial photodetectors reported in the literature. For example, InAs photodetectors have peak responsivities between $6.5 \times 10^2 \text{ A W}^{-1}$ and $1.3 \times 10^3 \text{ A W}^{-1}$ and detectivities of $3.0 \times 10^5 \text{ Jones}$ [63,64], InGaAs photodetectors have peak responsivities of $7.3 \times 10^3 \text{ A W}^{-1}$ and detectivities of $4.2 \times 10^{10} \text{ Jones}$ at 0.5 V [65,66] and PbS photodetectors exhibit peak responsivities and detectivities equal to 365.1 A W^{-1} and $1.4 \times 10^{12} \text{ Jones}$ at 10 V [67], $3 \times 10^{-3} \text{ A W}^{-1}$ and $7 \times 10^{10} \text{ Jones}$ at -1 V [68], and $1.0 \times 10^3 \text{ A W}^{-1}$ and $1.8 \times 10^{13} \text{ Jones}$ at 40 V [69], respectively. The different operating principle and material synthesis of the present detectors from those of commercial devices, make a direct quantitative comparison only partially representative. Given the early development stage of the dual-functionality IB detectors based on QCDs, we expect that the optimization of the design will lead to an improvement of the performance.

3. Conclusion

In conclusion, we demonstrated a path to dual-wavelength functionality from the same AR and device. We modeled the IB and ISB optical transitions in type-II InAs/AlSb QCDs on GaSb substrates and optically characterized the IB transitions of the devices by suppressing the ISB transitions with a lens for the SWIR regime, in the range of wavelengths between 1.83 μm and 2.50 μm , using an FTIR and a tungsten source. The devices have peak IB responsivities at zero bias between 2.8 mA W^{-1} and 24.8 mA W^{-1} at room temperature and specific detectivities between 2.56×10^7 Jones and 1.68×10^8 Jones. The application of an external bias voltage has been demonstrated to enhance the responsivity of the devices. For Device A, the increment is observed to reach up to 330 at a bias of 1.0 V and up to 360 at a bias of -1.0 V. The peaks have a blue shift under negative bias and a red shift under positive bias because of the displacement of the states in the band structure, as seen in the simulation results.

Funding. Air Force Office of Scientific Research (FA8655-23-1-7070, FA8655-25-1-7004); Austrian Science Fund (I 5772); H2020 European Research Council (853014); Österreichische Forschungsförderungsgesellschaft (904813).

Acknowledgment. The authors acknowledge the Center for Micro- and Nanostructures (ZMNS E057-12) at the TU Wien for access to the cleanroom facilities.

Disclosures. The authors declare no conflict of interest.

Data availability. The data that support the findings of this study are available from the corresponding author on a reasonable request.

Supplemental document. See [Supplement 1](#) for supporting content.

References

1. I. Coddington, N. Newbury, and W. Swann, "Dual-comb spectroscopy," *Optica* **3**(4), 414 (2016).
2. G. Villares, A. Hugi, S. Blaser, *et al.*, "Dual-comb spectroscopy based on quantum-cascade-laser frequency combs," *Nat. Commun.* **5**(1), 5192 (2014).
3. D. Hofstetter, J. Di Francesco, L. Hvozdar, *et al.*, "CO₂ isotope sensor using a broadband infrared source, a spectrally narrow 4.4 μm quantum cascade detector, and a Fourier spectrometer," *Appl. Phys. B* **103**(4), 967–970 (2011).
4. A. Harter, R. Szedlak, B. Schwarz, *et al.*, "Mid-infrared surface transmitting and detecting quantum cascade device for gas-sensing," *Sci. Rep.* **6**(1), 21795 (2016).
5. P. Dean, A. Valavanis, J. Keeley, *et al.*, "Terahertz imaging using quantum cascade lasers—a review of systems and applications," *J. Phys. D: Appl. Phys.* **47**(37), 374008 (2014).
6. Z. Wu, Y. Zhai, H. Kim, *et al.*, "Emerging Design and Characterization Guidelines for Polymer-Based Infrared Photodetectors," *Acc. Chem. Res.* **51**(12), 3144–3153 (2018).
7. Y.-G. Zhang, Y. Gu, X.-M. Shao, *et al.*, "Short-wave infrared InGaAs photodetectors and focal plane arrays," *Chin. Phys. B* **27**(12), 128102 (2018).
8. X. Guan, X. Yu, D. Periyangounder, *et al.*, "Recent Progress in Short- to Long-Wave Infrared Photodetection Using 2D Materials and Heterostructures," *Adv. Opt. Mater.* **9**(4), 2001708 (2021).
9. P. Yadav, S. Dewan, R. Mishra, *et al.*, "Review of recent progress, challenges, and prospects of 2D materials-based short wavelength infrared photodetectors," *J. Phys. D: Appl. Phys.* **55**(31), 313001 (2022).
10. F. Cao, L. Liu, and L. Li, "Short-wave infrared photodetector," *Mater. Today* **62**, 327–349 (2023).
11. P. Grant, S. Laframboise, R. Dudek, *et al.*, "Terahertz free space communications demonstration with quantum cascade laser and quantum well photodetector," *Electron. Lett.* **45**(18), 952–954 (2009).
12. H. Telle, G. Steinmeyer, A. Dunlop, *et al.*, "Carrier-envelope offset phase control: A novel concept for absolute optical frequency measurement and ultrashort pulse generation," *Appl. Phys. B* **69**(4), 327–332 (1999).
13. T. Udem, R. Holzwarth, and T. W. Hänsch, "Optical frequency metrology," *Nature* **416**(6877), 233–237 (2002).
14. J. Hillbrand, L. Matthieu Krüger, S. Dal Cin, *et al.*, "High-speed quantum cascade detector characterized with a mid-infrared femtosecond oscillator," *Opt. Express* **29**(4), 5774 (2021).
15. D. Hofstetter, M. Beck, and J. Faist, "Quantum-cascade-laser structures as photodetectors," *Appl. Phys. Lett.* **81**(15), 2683–2685 (2002).
16. L. Gendron, M. Carras, A. Huynh, *et al.*, "Quantum cascade photodetector," *Appl. Phys. Lett.* **85**(14), 2824–2826 (2004).
17. M. Graf, N. Hoyler, M. Giovannini, *et al.*, "InP-based quantum cascade detectors in the mid-infrared," *Appl. Phys. Lett.* **88**(24), 241118 (2006).
18. H. Schneider and H. C. Liu, *Quantum Well Infrared Photodetectors*, vol. 126 of *Springer Series in OPTICAL SCIENCES* (Springer Berlin Heidelberg, 2006).
19. A. Delga, "Quantum cascade detectors: A review," in *Mid-infrared Optoelectronics* (Elsevier, 2020), pp.337–377.

20. S. Sakr, E. Giraud, A. Dussaigne, *et al.*, “Two-color GaN/AlGaIn quantum cascade detector at short infrared wavelengths of 1 and 1.7 μm ,” *Appl. Phys. Lett.* **100**(18), 181103 (2012).
21. A. P. Ravikumar, T. A. Garcia, J. D. Jesus, *et al.*, “High detectivity short-wavelength II-VI quantum cascade detector,” *Appl. Phys. Lett.* **105**(6), 061113 (2014).
22. A. Vardi, G. Bahir, F. Guillot, *et al.*, “Near infrared quantum cascade detector in GaN/AlGaIn/AlN heterostructures,” *Appl. Phys. Lett.* **92**(1), 011112 (2008).
23. F. R. Giorgetta, E. Baumann, M. Graf, *et al.*, “Quantum Cascade Detectors,” *IEEE J. Quantum Electron.* **45**(8), 1039–1052 (2009).
24. H. C. Liu, C. Y. Song, A. J. SpringThorpe, *et al.*, “Terahertz quantum-well photodetector,” *Appl. Phys. Lett.* **84**(20), 4068–4070 (2004).
25. M. Graf, G. Scalari, D. Hofstetter, *et al.*, “Terahertz range quantum well infrared photodetector,” *Appl. Phys. Lett.* **84**(4), 475–477 (2004).
26. M. Krall, M. Martl, D. Bachmann, *et al.*, “Coupled cavity terahertz quantum cascade lasers with integrated emission monitoring,” *Opt. Express* **23**(3), 3581 (2015).
27. B. F. Levine, “Quantum-well infrared photodetectors,” *J. Appl. Phys.* **74**(8), R1–R81 (1993).
28. H. Schneider, C. Schönbein, G. Bihlmann, *et al.*, “High-speed infrared detection by uncooled photovoltaic quantum well infrared photodetectors,” *Appl. Phys. Lett.* **70**(12), 1602–1604 (1997).
29. V. Guériaux, A. Nedelcu, and P. Bois, “Double barrier strained quantum well infrared photodetectors for the 3–5 μm atmospheric window,” *J. Appl. Phys.* **105**(11), 114515 (2009).
30. A. M. Hoang, A. Dehzangi, S. Adhikary, *et al.*, “High performance bias-selectable three-color Short-wave/Mid-wave/Long-wave Infrared Photodetectors based on Type-II InAs/GaSb/AlSb superlattices,” *Sci. Rep.* **6**(1), 24144 (2016).
31. A. Dehzangi, R. McClintock, A. Haddadi, *et al.*, “Type-II superlattices base visible/extended short-wavelength infrared photodetectors with a bandstructure-engineered photo-generated carrier extractor,” *Sci. Rep.* **9**(1), 5003 (2019).
32. A. Dehzangi, J. Li, and M. Razeghi, “Band-structure-engineered high-gain LWIR photodetector based on a type-II superlattice,” *Light:Sci. Appl.* **10**(1), 17 (2021).
33. J. V. Li, R. Q. Yang, C. J. Hill, *et al.*, “Interband cascade detectors with room temperature photovoltaic operation,” *Appl. Phys. Lett.* **86**(10), 101102 (2005).
34. H. Lotfi, L. Li, L. Lei, *et al.*, “Short-wavelength interband cascade infrared photodetectors operating above room temperature,” *J. Appl. Phys.* **119**(2), 023105 (2016).
35. R. Q. Yang, Z. Tian, Z. Cai, *et al.*, “Interband-cascade infrared photodetectors with superlattice absorbers,” *J. Appl. Phys.* **107**(5), 054514 (2010).
36. Z. Tian, R. T. Hinkey, R. Q. Yang, *et al.*, “Interband cascade infrared photodetectors with enhanced electron barriers and *p*-type superlattice absorbers,” *J. Appl. Phys.* **111**(2), 024510 (2012).
37. Z.-B. Tian and S. Krishna, “Mid-Infrared Interband Cascade Photodetectors With Different Absorber Designs,” *IEEE J. Quantum Electron.* **51**(4), 1–5 (2015).
38. Z.-B. Tian and S. Krishna, “Mid-infrared metamorphic interband cascade photodetectors on GaAs substrates,” *Appl. Phys. Lett.* **107**(21), 211114 (2015).
39. H. Lotfi, L. Li, H. Ye, *et al.*, “Interband cascade infrared photodetectors with long and very-long cutoff wavelengths,” *Infrared Phys. Technol.* **70**, 162–167 (2015).
40. H. Lotfi, L. Lei, L. Li, *et al.*, “High-temperature operation of interband cascade infrared photodetectors with cutoff wavelengths near 8 μm ,” *Opt. Eng.* **54**(6), 063103 (2015).
41. L. Lei, L. Li, H. Ye, *et al.*, “Long wavelength interband cascade infrared photodetectors operating at high temperatures,” *J. Appl. Phys.* **120**(19), 193102 (2016).
42. W. Huang, L. Lei, L. Li, *et al.*, “Current-matching versus non-current-matching in long wavelength interband cascade infrared photodetectors,” *J. Appl. Phys.* **122**(8), 083102 (2017).
43. Z. Shen, Z. Yang, Z. Dai, *et al.*, “Multi-stage infrared detectors,” *Semicond. Sci. Technol.* **40**(3), 033001 (2025).
44. P. Martyniuk, A. Rogalski, and S. Krishna, “Interband Quantum Cascade Infrared Photodetectors: Current Status and Future Trends,” *Phys. Rev. Appl.* **17**(2), 027001 (2022).
45. R. Q. Yang, Z. Tian, J. F. Klem, *et al.*, “Interband cascade photovoltaic devices,” *Appl. Phys. Lett.* **96**(6), 063504 (2010).
46. P. Reininger, B. Schwarz, H. Detz, *et al.*, “Diagonal-transition quantum cascade detector,” *Appl. Phys. Lett.* **105**(9), 091108 (2014).
47. C. Koeniguer, G. Dubois, A. Gomez, *et al.*, “Electronic transport in quantum cascade structures at equilibrium,” *Phys. Rev. B* **74**(23), 235325 (2006).
48. P. Reininger, B. Schwarz, R. Gansch, *et al.*, “Quantum cascade detector utilizing the diagonal-transition scheme for high quality cavities,” *Opt. Express* **23**(5), 6283 (2015).
49. P. Reininger, T. Zederbauer, B. Schwarz, *et al.*, “InAs/AlAsSb based quantum cascade detector,” *Appl. Phys. Lett.* **107**(8), 081107 (2015).
50. A. Delga, M. Carras, L. Doyennette, *et al.*, “Predictive circuit model for noise in quantum cascade detectors,” *Appl. Phys. Lett.* **99**(25), 252106 (2011).

51. I. Vurgaftman, M. P. Lumb, and J. R. Meyer, *Bands and Photons in III-V Semiconductor Quantum Structures* (Oxford University Press, 2020), 1st ed.
52. M. Tchernycheva, L. Nevou, L. Doyennette, *et al.*, “Systematic experimental and theoretical investigation of intersubband absorption in GaN/AlN quantum wells,” *Phys. Rev. B* **73**(12), 125347 (2006).
53. M. Giparakis, H. Knötig, H. Detz, *et al.*, “2.7 μm quantum cascade detector: Above band gap energy intersubband detection,” *Appl. Phys. Lett.* **120**(7), 071104 (2022).
54. M. Giparakis, A. Windischhofer, S. Iseri, *et al.*, “Design and performance of GaSb-based quantum cascade detectors,” *Nanophotonics* **13**(10), 1773–1780 (2024).
55. P. Reininger, B. Schwarz, A. Harrer, *et al.*, “Photonic crystal slab quantum cascade detector,” *Appl. Phys. Lett.* **103**(24), 241103 (2013).
56. B. Schwarz, P. Reininger, A. Harrer, *et al.*, “The limit of quantum cascade detectors: A single period device,” *Appl. Phys. Lett.* **111**(6), 061107 (2017).
57. G. Marschick, M. David, E. Arigliani, *et al.*, “High-responsivity operation of quantum cascade detectors at 9 μm ,” *Opt. Express* **30**(22), 40188 (2022).
58. S. Kalchmair, H. Detz, G. D. Cole, *et al.*, “Photonic crystal slab quantum well infrared photodetector,” *Appl. Phys. Lett.* **98**(1), 011105 (2011).
59. S. C. Lee, S. Krishna, and S. R. J. Brueck, “Quantum dot infrared photodetector enhanced by surface plasma wave excitation,” *Opt. Express* **17**(25), 23160 (2009).
60. F. Capasso, N. Yu, E. Cubukcu, *et al.*, “Using Plasmonics to Shape Light Beams,” *Opt. Photonics News* **20**(5), 22 (2009).
61. A. Harrer, B. Schwarz, R. Gansch, *et al.*, “Plasmonic lens enhanced mid-infrared quantum cascade detector,” *Appl. Phys. Lett.* **105**(17), 171112 (2014).
62. A. Windischhofer, N. Opačak, and B. Schwarz, “Charge Transport in Interband Cascade Lasers: An Ab-Initio Self-Consistent Model,” *Laser Photonics Reviews* **19**(3), 2400866 (2025).
63. J. Miao, W. Hu, N. Guo, *et al.*, “High-Responsivity Graphene/InAs Nanowire Heterojunction Near-Infrared Photodetectors with Distinct Photocurrent On/Off Ratios,” *Small* **11**(8), 936–942 (2015).
64. Y. Yang, X. Peng, H. S. Kim, *et al.*, “Hot Carrier Trapping Induced Negative Photoconductance in InAs Nanowires toward Novel Nonvolatile Memory,” *Nano Lett.* **15**(9), 5875–5882 (2015).
65. Z. Liu, T. Luo, B. Liang, *et al.*, “High-detectivity InAs nanowire photodetectors with spectral response from ultraviolet to near-infrared,” *Nano Res.* **6**(11), 775–783 (2013).
66. R. Pokharel, P. Ramaswamy, S. Devkota, *et al.*, “Epitaxial High-Yield Intrinsic and Te-Doped Dilute Nitride GaAsSbN Nanowire Heterostructure and Ensemble Photodetector Application,” *ACS Appl. Electron. Mater.* **2**(9), 2730–2738 (2020).
67. W. Chen, H. Tang, Y. Chen, *et al.*, “Spray-deposited PbS colloidal quantum dot solid for near-infrared photodetectors,” *Nano Energy* **78**, 105254 (2020).
68. I. Ka, L. F. Gerlein, I. M. Asuo, *et al.*, “Solution-Processed p-Type Copper Thiocyanate (CuSCN) Enhanced Sensitivity of PbS-Quantum-Dots-Based Photodiode,” *ACS Photonics* **7**(7), 1628–1635 (2020).
69. G. Konstantatos, I. Howard, A. Fischer, *et al.*, “Ultrasensitive solution-cast quantum dot photodetectors,” *Nature* **442**(7099), 180–183 (2006).